# THE EFFECT OF TOW GAPS ON COMPRESSION AFTER IMPACT STRENGTH OF AFP LAMINATES

A. T. Rhead[1], T. J. Dodwell[1], R. Butler[1]*

[1]*Department of Mechanical Engineering, University of Bath, Claverton Down, Bath, BA2 7AY, UK*
*\*R.Butler@bath.ac.uk*

**Keywords:** Impact, delamination, strength, tow-steering.

**Abstract**
*When Automated Fibre Placement (AFP) is used to manufacture aerospace components with complex three dimensional geometries, gaps between fibre tows can occur. This paper explores the interaction of these tow gaps with impact damage. Impact of two coupons containing tow gaps shows that the area of delamination is smaller for an impact directly over a tow gap where the tow gap lies close to the non-impact face. Compression After Impact (CAI) testing shows that both the formation of sublaminate buckles and subsequent growth of delaminations is inhibited by the presence of a tow gap near the non-impact face. Non-destructive testing techniques and a computationally efficient infinite strip model are used to analyse the damage resistance and damage tolerance of the coupons.*

## 1 Introduction

Automated fibre placement (AFP) technologies [1] allow the rapid production of CFRP structures. In current AFP processes, the tow placement head is constrained to remain perpendicular to the direction in which tows are laid [2]; thereby ensuring each course of tows maintains a constant ply thickness. This allows courses of straight fibre tows to be laid down efficiently on flat or gently curved surfaces. However, parts with more complex geometries require tows to be steered. In these more complex cases, the restraint of the fibre placement head can cause gaps or overlaps to form between courses. This is demonstrated in the following example of a tapered channel section, Fig. 1(a).

Such sections are a representation of the principal load carrying structures which run from the root to the tip of an aircraft wing. It is manufactured by building up courses of AFP tows over a mandrel tool. A tapered channel section comprises flanges (F1 and F2) and a web (W). As each flange is predominately loaded in shear, the precise alignment of $45^o$ fibres in these regions is important. The channel cross section changes along its length as a result of a taper in the wing, Fig. 1(b), meaning flange F2 lies at an angle of $\theta^o$ to flange F1. If an AFP machine started by laying a straight $45^o$ course of tows across F1, the course of tows would remain at $45^o$ on web W, yet would be at $45 + \theta^o$ on flange F2. With restriction of the AFP head in mind, the approach taken is to sacrifice the fibre angle over the web by steering tows through an angle $\theta^o$ across W. This ensures that both flanges F1 and F2 will have fibres at $45^o$. To understand this first consider two courses, each of 8 tows, being laid adjacent to one another without gaps. The constraint that the normal thickness of the layers must remain constant, coupled with no gaps being allowed between courses, forces the curvature of

consecutive tows to tighten, quickly leading to a non-manufacturable *geometric singularity* [3,4], see Fig. 2(a). Even before this singularity, there is a limit to the curvature which an AFP head can produce. High curvatures lead to extra compression being induced on the inner side of the course, making tows susceptible to micro-buckling and other defects. The current solution is a compromise of laying identical courses of curved tows adjacent to one another but allowing gaps to form between each course, as shown in Fig. 2(b).
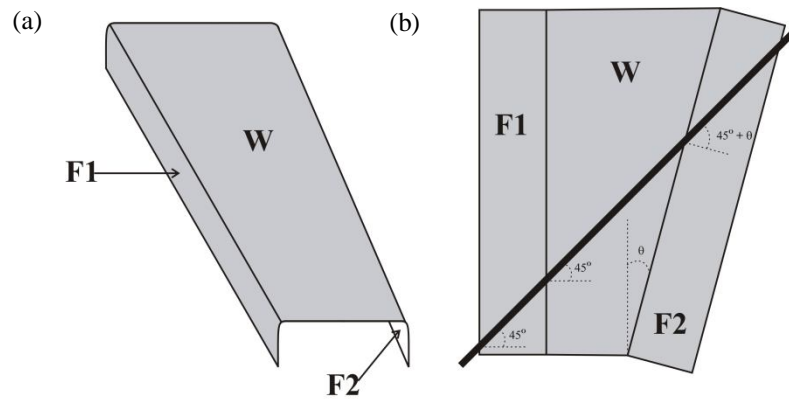


**Figure 1** (a) Shows a typical configuration of channel section with a tapering cross-section. (b) Shows an unfolded view of the channel demonstrating the path of a 45° fibre. Note that the path does not remain at 45° over surface S2.
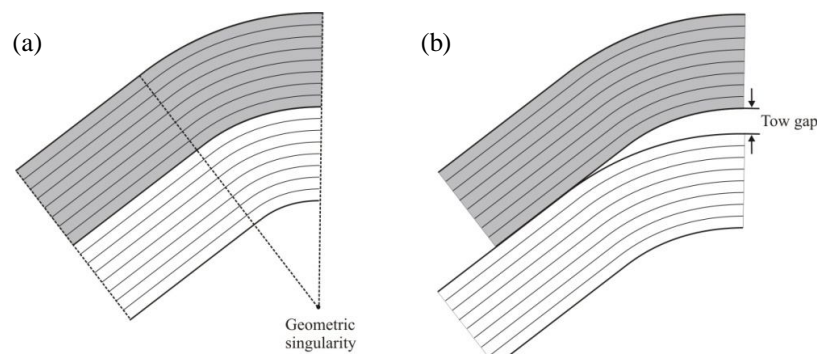


**Figure 2** Two possible configurations for adjacent courses of 8 steered tows. (a) Courses are laid down so that no gaps form between each course, consequently the curvature of each consecutive tow is force to tighten. (b) By laying down identical courses next to one another, no such tightening of curvatures occurs, but at the sacrifice of gaps between courses.

In-service components with tow gaps may be subject to impact damage which is mainly comprised of intra-ply cracks and delaminations. Therefore the study of the effect of ply gps and post impact performance is of interest. Barely visible impact damage (BVID) is a particular form of impact damage that causes surface deformations just below the limit of detectability on a standard visual inspection of an in-service aircraft. Under compressive loading BVID may spread ultimately causing failure of the component. Currently, this is prevented by setting a damage tolerance strain allowable for the component below the strain required to cause delamination propagation. However, if any reduction were required in the damage tolerant strain allowable due to the presence of tow gaps, the structure would need to be thickened. This would result in an increase in aircraft weight at the cost of fuel efficiency.

The effect of impact on aircraft components falls into two categories, damage resistance (how much damage is incurred for a given impact) and damage tolerance or compression after impact (CAI) strength (the amount of strain the damaged structure can tolerate before failure),

both of which are interlinked and studied in this paper. This paper will show that impact of a coupon directly over a tow gap close to the non-impact face, where all the delaminations likely to propagate under compressive loading form, produces a smaller damage area than impact to a region with a tow gap near the impact surface. Subsequent CAI testing shows that tow gaps near the non-impact surface can also inhibit sublaminate buckling and growth of delaminations.

## 2 The Strip model of sublaminate buckling and delamination

The Strip model [5] predicts critical threshold values of compressive axial strain below which local sublaminate buckling-driven propagation of delaminations will not occur. It is assumed that the boundaries of the delaminations being considered are circular or can be approximated by a circle [6]. The Strip model is an equivalent model that does not represent exact physical reality. Instead it seeks to retain the equivalent value of elastic energy stored in the post-buckled sublaminate while releasing it in pure Mode I (peeling regime); a simplification of the mixed mode conditions detected in the full 3D reality. A comparison of bending and membrane energies in the sublaminate prior to and following propagation [6] is used to derive an equation for the threshold strain, $\varepsilon_{th}$, the strain below which delamination propagation will not occur,

$$\varepsilon_{th} = \varepsilon^C \left( \sqrt{4 + \frac{2G_{IC}}{(\varepsilon^C)^2 A_{11}}} - 1 \right) \qquad (1)$$

Here $A_{11}$ is the axial stiffness of the sublaminate, $G_{IC}$ is the strain energy release rate required to cause Mode I failure of the matrix and $\varepsilon^C$ is the sublaminate buckling strain calculated using the infinite strip program VICONOPT [7]. Other methods for calculating the buckling strain such as FEA can be used, however this is likely to result in a considerable loss in computational efficiency. A useful description of the Strip model using an equivalent sandwich strut analogy is given in [8] and a full derivation can be found in [5]. Note that, the number of plies making up the sublaminate is assumed to remain constant.

## 3 Materials and test methods

Two coupons were cut from an area of a tapered channel section with stacking sequence $[\pm 45/0/-45/90/0_2/45/0_2/\pm 45/0_2/45/0_2/90/-45/0/\mp 45]$. The channel was manufactured from 0.25mm thick Hexcel M21/IMA-12k pre-preg CFRP tows with material properties $E_{11} = 145$GPa, $E_{22} = 8.5$GPa, $G_{12} = 4.2$GPa, $v_{12} = 0.35$ and $G_{IC} = 500$J/m$^2$. The Coriolis Composites AFP machine used to manufacture the channel section lays courses of up to 8 tows at a time with a total width of 50.1mm per course. Coupon dimensions and a diagram of areal tow gap positions for both coupons A and B are given on the right hand side of Fig. 3. A photographic cross-section of a tow gap in the 8<sup>th</sup> (45°) ply of coupon B together with surface images taken using an Ultrasonic Sciences Ltd C-scan system showing tow gaps in the vicinity of the impact point (central to the image) can be seen in Fig. 4. As a consequence of the consolidation of plies in the manufacturing process, tow gaps manifest themselves as approximately 3mm wide and 0.25-0.5mm deep channels on the free (non-tool) surface of coupon B. The tow gap seen in the centre of Fig. 4(c) occurs in the 14<sup>th</sup> ply. The distance of this tow gap from the free surface means little surface distortion is present in comparison to coupon B. This can be seen as a comparative lack of definition of the gap in Fig. 4(b). Further channels are seen in coupon A but occur in the first ply and hence are present on the free surface only. No channels are present on the tool surface of either coupon.

Coupons were subject to 18J impacts at the plan form centre of their flat tool surface. Impacts were delivered by an Instron Dynatup 9250 HV instrumented drop weight impact machine employing a 16mm hemispherical tup. Coupons were held during impact across a 125 mm by 75 mm window as per ASTM standard D7137 [9]. Coupons were C-scanned following impact to establish the induced damage morphology.
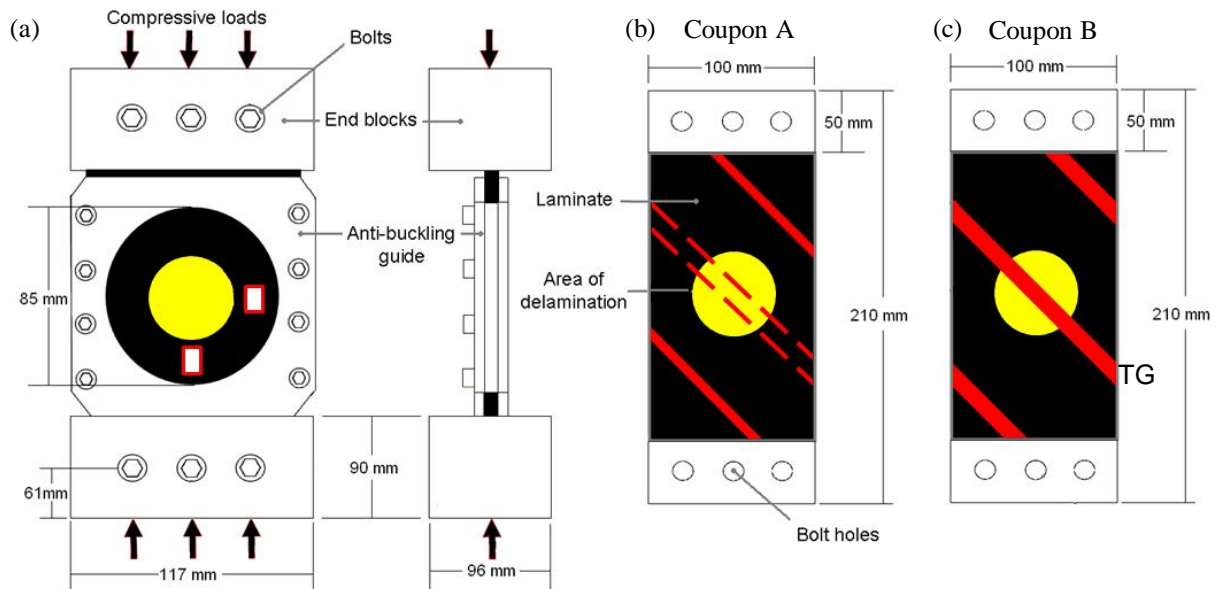


**Figure 3.** (a) Compression after impact test fixture, (b) and (c) schematics of coupons A and B respectively showing areal positioning of tow gaps and impact sites on the free surface. TG indicates the position of the photographic cross-section in Fig. 4(a).
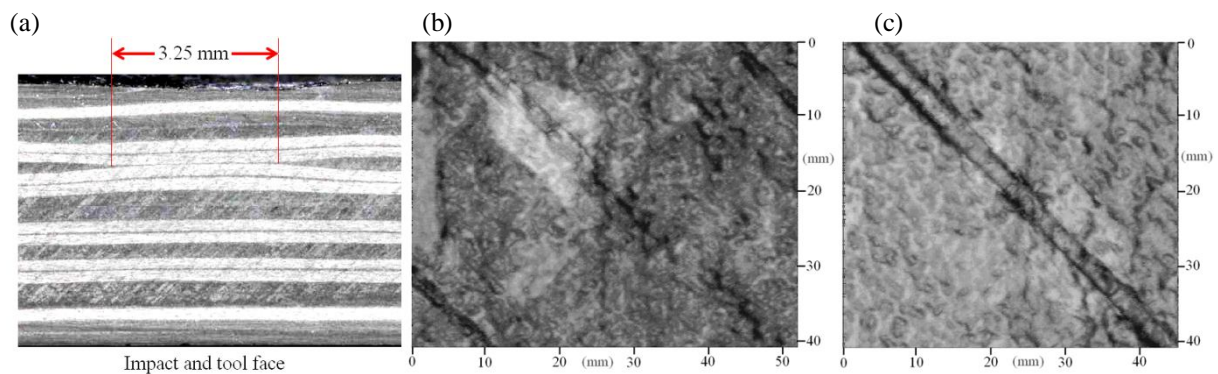


**Figure 4.** Tow gaps images: (a) cross-section photograph of the edge of coupon B at point TG in Fig. 3(c) showing a tow gap in the 8th layer. (b) and (c) C-scan surface images of A and B respectively.

They were subsequently subject to compression to failure in an Instron 5585H compression test machine at an axial displacement rate of 0.1 mm/min. During compression, the coupons were restrained against overall buckling by an anti-buckling guide see Fig. 3(a). A Digital Image Correlation (DIC) system, employing a pair of stereo cameras was used to measure the 3D surface displacement of the laminates in relation to their unloaded position. This allowed the visualization of buckling modes and delamination growth following post-processing. To ensure panels were correctly aligned and placed under pure axial compression, strains were recorded throughout the tests by two pairs of vertically aligned back-to-back strain gauges, see Fig. 3(a).

## 4 Results

### *4.1 Impact results*

Coupons were nominally impacted at 18J. However a comparison of impact plots for coupons A and B in Fig. 5 shows that the peak energy received was 18.1 J and 18.6 J for coupons A and B respectively. Areas under the energy curves in Fig. 5 and peak deflection data indicates that coupon B exhibited a more elastic response to impact. Peak impact loads were 9.6 kN and 9.4 kN for coupons A and B respectively. Post-impact C-scan images are shown in Figs 6(a), (b), (d) and (e). Figures 6 (a) and (d) show surface damage to the tool surface following impact and Figs 6 (b) and (e) show the extent of delamination for each coupon.
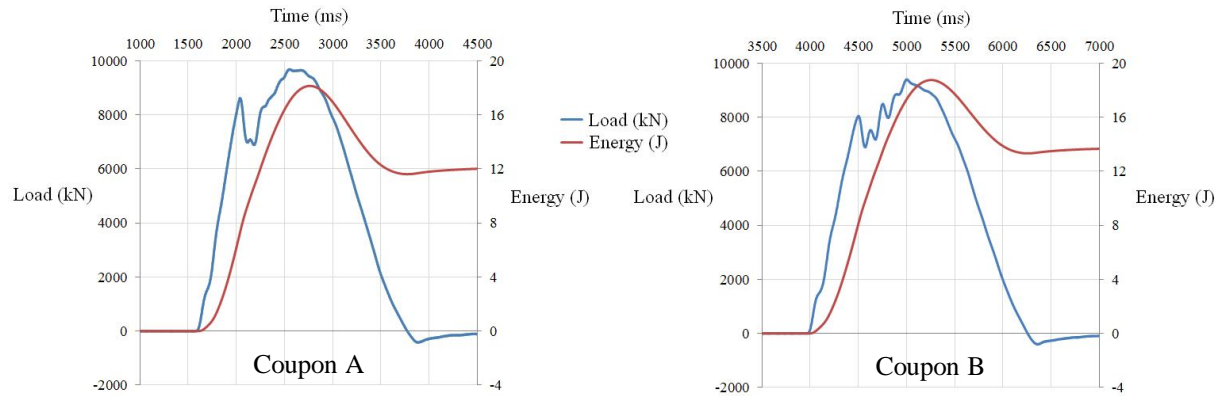


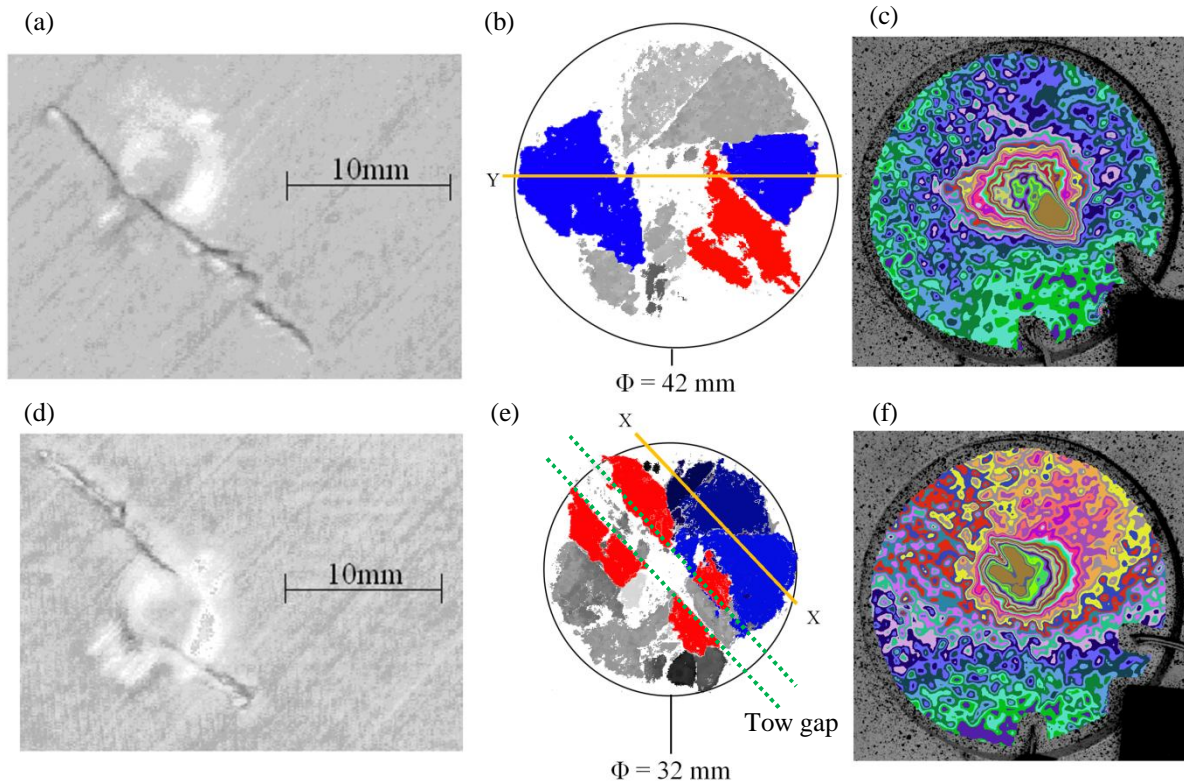**Figure 5.** Impact load and energy versus time plots.



**Figure 6.** (a) and (d) surface C-scan images of impact sites, (b) and (e) time-of-flight C-scan images of impact damage in coupons A and B respectively. Red areas indicate delaminations involved in the 1st sublaminate buckle and blues areas relate to those involved in the second sublaminate buckling events. (c) and (f) DIC images at 184kN and 211kN of sublaminate buckles immediately prior to propagation for coupons A and B respectively.

Highlighted delaminations are those related to sublaminates which subsequently buckle under compressive loading. C-scan images of the impact surfaces of A and B shown in Figs. 6 (a) and (d) indicate that surface damage was of an order of visibility consistent with BVID. As shown in Figs. 6(b) and (e) the full delamination area for coupon A is larger than for coupon B. Delamination morphologies appear to be similar for both coupons although the presence of a tow gap in coupon B can easily be seen on Fig. 6 (e).

### 4.2 Compression after impact results

For all DIC images, colours show changing out-of-plane displacement from an unloaded reference state. Thin well defined contours indicate a steep gradient, see Fig. 6. Different sublaminate buckling events were detected in each coupon test. The sublaminate relating to the smaller 1<sup>st</sup> interface delamination (red delaminations in Figs. 6 (b) and (e)) was the first to buckle in both coupons. In coupon B buckling was clearly constrained by the tow gap running through the centre of the laminate, see Fig. 6(e). Similarly, the formation of the second sublaminate buckling mode in coupon B (blue delaminations, Fig. 6(e)) was inhibited by the same tow gap, (see Fig. 3(c) and 6(f)). No interference of sublaminate buckling by tow gaps was seen in coupon A. Comparison of C-scan and DIC images in Fig. 6 shows that the formation of the 2<sup>nd</sup> sublaminate buckle in coupon B occurs above a number of different delaminations. In contrast, a comparison of Figs. 6 (b) and (c) indicates that the second sublaminate buckle in coupon A formed when two delaminations at the 4<sup>th</sup> interface coalesced. Based on sections through XX and YY in Figs. 6 (b) and (e), Fig. 7 shows an idealized cross-sectional representation of the layers involved in the second sublaminate buckling mode for each coupon. Failure occurred in both laminates following the formation of the 2<sup>nd</sup> sublaminate buckling event as a consequence of unstable delamination propagation [10].
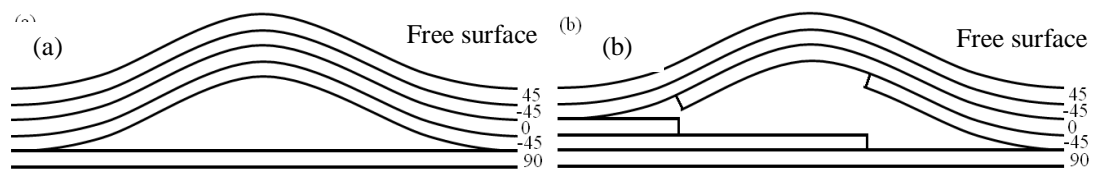


**Figure 7.** (a) and (b) Idealized schematics of sections YY and XX from Figs 6(b) and (e) respectively following the second sublaminate buckling event in each coupon.

Figure 8 gives experimental and analytical sublaminate buckling and delamination propagation results for both coupons based on delamination diameters derived from Figs. 6(b) and (e).
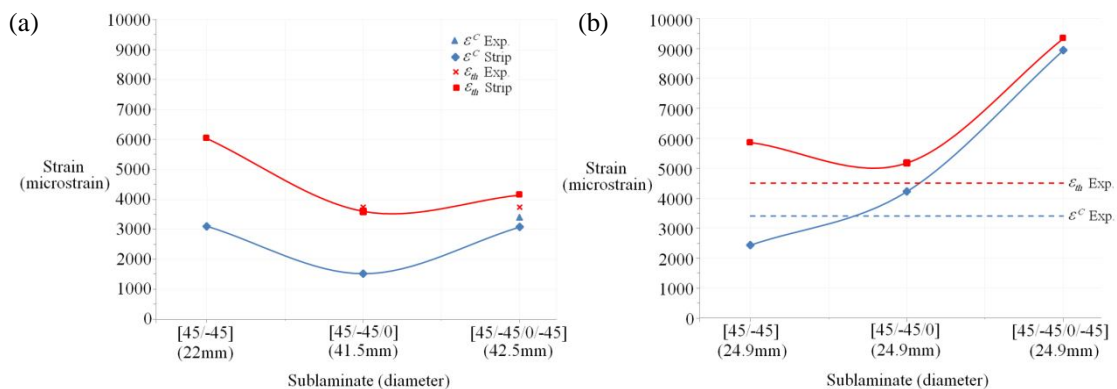


**Figure 8.** Experimental and analytical sublaminate buckling and delamination propagation strains for the outer 2, 3 and 4 ply sublaminates of coupon (a) A and (b) B. Diameters of delamination considered in the analysis are given in brackets.

Experimental strains were calculated by correlating average strain gauge readings with DIC images (see Figs 6 (c) and (f)) using the load output of the compression test machine.
The average of the strain gauge readings was used as it accounts for losses in stiffness during the tests.

*4.3 Analytical results*

VICONOPT sublaminate buckling strains in Fig. 8 are based on a circular approximation of the full extent of the delaminations involved. The diameter of this circle is determined by using DIC images to pinpoint the delaminations involved then correlating these with C-scans taken prior to compression to accurately determine delamination extent; contrast all images in Fig. 6. A comparison of Figs 6(e) and (f) indicates that the $2^{nd}$ sublaminate buckling event in coupon A involved a sublaminate with areas that were two, three and four plies thick. Hence for coupon A, as a bounding approximation to the actual multi-thickness sublaminate, results are given for sublaminates consisting of 2, 3 and 4 continuous plies, see Fig. 8(a). Corresponding values of threshold strain are given for each of the sublaminates using the associated values of $A_{11}$. For coupon B analytical results are given for sublaminates [45] and [ ±45/0/-45] (red and blue areas on Fig. 6(e)) as these can be seen to buckle on the DIC images, see Figs 6(e) and (f).

**5 Discussion**

The position, width and depth of tow gaps appear to be significant for damage resistance. A comparison of C-scans in Figs. 6(b) and (e) shows that the presence of a tow gap near the free surface directly under the point of impact results in a smaller total area of delamination in coupon B than in coupon A. It is suggested that the difference in extent of delaminations between coupons A and B may be a consequence of the tow gap acting as a crack blunter; impeding the spread of delaminations in Mode II. Additionally, the tow gap may inhibit through-thickness shearing during impact, particularly near the non-impact face. This may be why the tow gap in coupon B was more effective at improving damage resistance than the one in coupon A. The marginally increased elastic response to impact noted in coupon B may also, to some extent, account for the smaller delaminations seen in this coupon. However, as coupons were otherwise identical, this elasticity is likely to have been a consequence of the tow gap. It remains to be seen whether this improved resistance will apply to impact in the vicinity of a tow gap.

A comparison of DIC and C-scan images clearly shows that the first sublaminate buckle in both coupons contains only a single ply. The delaminations relating to these sublaminates both failed to propagate following buckling. The split in the buckling modeshape of the single ply sublaminate in coupon B is due to the interference of the tow gaps in the $1^{st}$ and $8^{th}$ plies from the free surface.

Results in Fig. 8 indicate that failure occurred at higher applied strain for coupon B than coupon A suggesting that tow gaps near the free surface may be beneficial for damage tolerance. It is suggested that this is either a consequence of the smaller total area of impact damage in coupon A or the result of the tow gap preventing the delaminations at the $4^{th}$ interface from joining up as in the core of coupon A. Both of these possibilities are linked to the presence of a tow gap near the free surface under the point of impact. It is noted that comparisons should be made with a CAI test on a coupon that is free of tow gaps. This will determine whether some configurations of tow gaps actually improve damage tolerance or merely offer smaller losses in CAI strength. The prediction of threshold propagation strain for the delamination associated with the second sublaminate to buckle in coupon A was within

11% of the experimental value. A comparison of analytical and experimental results in Fig.8 (b) shows that the strain at which the $2^{nd}$ sublaminate buckling event in coupon B occurred is bounded by analytical predictions for buckling of the $2^{nd}$ and $3^{rd}$ ply continuous sublaminates. Analytical propagation results for the 3 ply sublaminate are within 15% of the experimental result. Delamination propagation is often linked to the presence of $0^o$ plies in the associated sublaminate. Interchanging the $0^o$ ply for a $45^o$ ply in the area where sublaminates buckled may have improved damage tolerance [10].

## 6 Conclusions

Two coupons containing tow gaps were subject to CAI testing. Tow gaps in coupon B were located directly under the impact site near the non-impact surface, the region where the delaminations most likely to propagate form during impact, and caused significantly more surface deformation than in coupon A. The surprising result was that impact damage was less severe for coupon B. Equally surprising was that damage tolerance was also better for coupon B as both delamination formation during impact and delamination growth during compressive loading were inhibited. However, further work is required to ascertain what effect the presence of tow-gaps in the vicinity of an impact (rather than directly below it) will have on damage resistance and damage tolerance. In particular, a CAI test of a control coupon devoid of tow gaps should be undertaken. Future models of sublaminate buckling and delamination propagation should consider the possibility of a sublaminate with discontinuous plies.

## Acknowledgements

## References

[1] Croft, K., Lessard, L., Pasini, D., Hoijati, M., Chen, J. H., Yousefpour A. Experimental study of the effect of automated fibre placement induced defects on performance of composite laminates. *Compos Part A: Appl. Sci. Manuf.*, **42**(5), pp. 484-491 (2011)

[2] Kim, B. C, Potter, K., Weaver, P. Continuous tow shearing for manufacturing variable angle tow composites. *Compos Part A: Appl. Sci. Manuf.* (2012). (doi:10.1016/j.compositesa.2012.02.024) (Accepted)

[3] Peletier, M. A., Veneroni, M. Stripe patterns and a projection-valued formulation of the eikonal equaton. *Phil. Trans. R. Soc. Lond. A.*, **370**, pp. 1730-1739 (2012).

[4] Dodwell, T. J., Hunt G. W., Peletier, M. A., Budd, C. J. Multi-layered folding with voids. *Phil. Trans. R. Soc. Lond. A.*, **370**, pp. 1740-1758 (2012).

[5] Butler, R., Rhead, A. T., Liu, W., Kontis, N. Compressive strength of delaminated aerospace composites. *Phil. Trans. R. Soc. Lond. A.* **370**(1965), pp.1721-2026 (2012).

[6] Rhead, A.T., Butler R. Compressive static strength model for impact damaged laminates. *Compos. Sci. Technol.* **69**(14), pp. 2301-2307 (2009).

[7] Williams F.W., Kennedy D., Butler R., Anderson M.S. VICONOPT – Program for exact vibration and buckling analysis or design of prismatic plate assemblies. *AIAA*, **29**(11), pp. 1927 -1928 (1991).

[8] Rhead A.T., Butler R., Hunt G.W. Compressive strength following delamination induced interaction of panel and sublaminate buckling. Proceedings of *53<sup>rd</sup> AIAA SDM conference,* Waikiki, Hawaii, USA, 2012 (accepted).

[9] ASTM D7136 / D7136M – 07. Standard test method for measuring the damage resistance of a fiber-reinforced polymer matrix composite to a drop-weight impact event, (2009), doi:10.1520/ D7136_D7136M-07.

[10] Rhead, A. T., Butler, R. and Baker, N. Analysis and compression testing of laminates optimised for damage tolerance. *Applied Composite Materials*, **18** (1), pp. 85-100. (2011)